Enhanced epitaxial growth of two-dimensional monolayer WS$_2$ film with large single domains

Changyong Lan [a,b,*], Rui Zhang [a,b], Haolun Wu [a,b], Shaofeng Wen [a,b], Ruisen Zou [a,b], Xiaolin Kang [c], Chun Li [a,b,e,*], Johnny C. Ho [c,d,*], Yi Yin [a,b], Yong Liu [a,b]

[a] State Key Laboratory of Electronic Thin Films and Integrated Devices, University of Electronic Science and Technology of China, Chengdu 611731, China
[b] School of Optoelectronic Science and Engineering, University of Electronic Science and Technology of China, Chengdu 611731, China
[c] Department of Materials Science and Engineering, and State Key Laboratory of Terahertz and Millimeter Waves, City University of Hong Kong, Hong Kong 999077, China
[d] Key Laboratory of Advanced Materials Processing & Mold (Zhengzhou University), Ministry of Education, Zhengzhou University, Zhengzhou 450002, China
[e] Wuhan National Laboratory for Optoelectronics, Huazhong University of Science and Technology, Wuhan 430074, China

A R T I C L E   I N F O

A B S T R A C T

The emerging of graphene has stimulated the exploration of two-dimensional (2D) nanomaterials. As a kind of important semiconducting 2D materials, WS$_2$ shows great potentials in electronics, optoelectronics, and photonics, *etc.*; however, the synthesis of high quality, large area, uniform and epitaxial 2D WS$_2$ monolayer films is still a challenge. Herein, we report the epitaxial growth of WS$_2$ on sapphire with excellent electrical and optoelectronic properties *via* an enhanced chemical vapor deposition method. With the assistance of Na$_2$WO$_4$ as well as the investigation of related growth mechanism, large single crystal triangular WS$_2$ monolayer flakes with well-defined orientations are achieved. The corresponding single crystal domain size is larger than 1 mm together with the centimeter-scale continuous film realized. Once fabricated into transistors, the monolayers exhibit excellent device properties, such as high mobility and large on/off current ratio. Also, these devices give respectable photoresponse properties when operated in the photoconductive mode. The peak responsivity can reach 4.6 A W^{-1}. All these results demonstrate the high quality of as-synthesized WS$_2$ monolayers, indicating the bright future of this synthesis technology for 2D materials towards practical applications.

1. Introduction

Due to the fascinating properties, two-dimensional (2D) nanomaterials with the atomic thickness have been widely demonstrated with excellent electrical and photoelectric characteristics for promising utilization in electronics, and optoelectronics, *etc.* [1–4]. Since there are a broad range of materials within the 2D family, including insulators, semiconductors, semimetals, and superconductors [5], different 2D monolayers can be heterogeneously integrated as both active and passive materials to build complete sets of devices, where their ultra-thin natures are advantageous for flexible and wearable applications [6]. Even compared to silicon, the "workhorse" of the electronic industry, 2D monolayers, such as MoS$_2$ and WS$_2$, exhibit superior semiconducting properties [2,3], being capable to serve as ideal alternative active channel materials in the post-Si era.

For practical applications, the use of 2D materials inevitably requires reliable synthesis methods, especially to achieve the large-area, uniform, crystalline and epitaxial monolayer films; however, it is still a great challenge to realize these demanding synthesis techniques [7,8]. Among various synthesis schemes, chemical vapor deposition (CVD) is one of the most promising and cost-effective schemes to obtain large-scale and high-quality 2D materials [8,9]. In fact, during the past decade, there is a lot of pioneer works carried out towards the large-area and high-quality synthesis of 2D materials by different CVD methods. Particularly, Xu and his team realized the meter-sized single-crystalline graphene on industrial copper foils employing the CVD method [10]. Yu et al. reported the synthesis of large-area highly-oriented MoS$_2$ monolayer films by the CVD technique [11]. Later, the same group achieved the wafer-scale MoS$_2$ monolayers with large single crystal domains employing the modified CVD method [12]. In contrast to MoS$_2$, WS$_2$ is another important semiconducting transition metal dichalcogenide 2D materials, but its large-scale epitaxial synthesis is still far lack behind although there are recent advances in various growth methods [13]. For example, Zhou and his group ex-

plored the fast growth of WS_2 flakes (*i.e.* not necessarily mono-layers) with the single crystal size reaching 500 μm using K_2WS_4 as the growth precursor [14]. Gao et al. revealed that the very large single crystal size of WS_2 up to 1 mm could be potentially achieved by simply using Au foils as substrates [15]. Ji and his team found that the introduction of hydrogen could facilitate the epitaxial growth of monolayer WS_2 triangles on c-oriented sapphire substrates owing to the increased interaction between WS_2 and sapphire [16]. Nonetheless, the obtained single crystal size is relatively small with the lateral dimension of only around 3 μm, which significantly hinders its use for constructing large-scale devices. Epitaxial WS_2 monolayers with low in-plane rotational twist was lately achieved by Chubarov et al. using metalorganic CVD method with a multistep growth process [17]. Although unidirectional WS_2 monolayers have been achieved, the single domain WS_2 flakes are very small ($\sim$200 nm), resulting in large numbers of grain boundaries. Thus, epitaxial WS_2 monolayers with large single domains are highly preferred.

It has been reported that several inorganic salts, such as NaCl and KCl, can be exploited to reduce the melting point of metal oxides, facilitating the evaporation of metal source, and realizing the synthesis of various kinds of 2D materials [18]. In any case, it is difficult to have a rational control on the evaporation rate of metal oxides, which always leads to the formation of thick 2D materials. In this work, we demonstrate the successful synthesis of well-oriented large single domain size of WS_2 monolayer films by a modified CVD method. In the synthesis, mixed powders of WO_3 and $Na_2WO_4 \bullet 2H_2O$ were employed as the W source. With the assistance of $Na_2WO_4 \bullet 2H_2O$, the evaporation of W source can be well controlled, leading to the formation of large monolayer single crystal WS_2 triangular grains and subsequently uniform WS_2 monolayer films. Importantly, the as-synthesized single crystal triangular grains have well-aligned orientations to ensure the in-plane texture uniformity. When fabricated into simple back-gated devices, the obtained WS_2 monolayers exhibit decent electrical and photodetection performance, illustrating their promising applications in next-generation electronics and optoelectronics.

2. Materials and methods

2.1. Materials synthesis

For the synthesis of WS_2 monolayer films, a single heating zone furnace was utilized. The details of the setup can be found in Supporting Information Figure S1. To be specific, a quartz tube with diameter of 1 inch was used as the reaction chamber for the material growth. Mixed powders (800 mg) of WO_3 (99.8%, Xiya Reagent) and $Na_2WO_4 \bullet 2H_2O$ (99.5%, Macklin) with different mass ratios were exploited as the W source, where they were placed in a quartz boat. The quartz boat was then positioned in the center of the heating zone. At the same time, 300 mg of S powder (99.95%, Aladdin) was employed as the S precursor, being placed in a corundum boat. The corundum boat was housed in the upstream side of the quartz tube, sitting outside of the heating zone. In this case, a heating belt was used to heat the S powder during the reaction while the temperature of the heating belt was set to be 150 °C. Several pieces of single side polished c-oriented sapphire were applied as the substrates, which were placed in the downstream side of heating zone of the furnace. Before heating, the pressure inside the quartz tube was first pumped to 1 Pa by a mechanical pump. Next, high purity Ar gas (99.999%) was introduced into the tube with a flow rate of 200 sccm. During the reaction, the pressure inside the quartz tube was maintained at about 140 Pa monitored by a pressure gage (901p-11040, mks). The furnace was heated to 930 °C in 30 min and kept at that temperature for 60 min. After

the reaction, the furnace was cooled to room temperature naturally under Ar flow.

2.2. Characterization

The thermogravimetry and differential scanning calorimetry analysis of the precursors are performed with a thermal analyzer (STA 449 F3 Jupiter, NETZSCH). After the synthesis, the obtained WS_2 films were inspected by an optical microscope (BX53, Olympus) and a scanning electron microscope (SEM, VEGA3 SBH, TESCAN). An atomic force microscope (AFM, FM-Nanoview 1000, FSM-Precision) was used to examine the thickness of the WS_2 film. The Raman and PL spectra of the WS_2 films were collected by a spectrometer (SR-500i-A-R, Andor) with a 532 nm excitation laser. The excitation power was fixed at 2 mW for the PL and Raman measurements. A fiber-spectrometer (BLK-C-SR, Stellar Net Inc) with deuterium halogen light source (SL5-CUV, Stellar Net Inc) was utilized to measure the absorbance of the WS_2 films. For the absorbance measurements, the WS_2 films were transferred onto a glass substrate using polystyrene as the protecting layer [19,20]. A transmission electron microscope (TEM, 200 kV, Tecnai G2 F20, FEI) was used to assess the crystal structure and crystallinity of the WS_2 films.

2.3. Devices fabrication and measurements

For the device fabrication, the as-synthesized WS_2 films were transferred from the sapphire substrate to the SiO_2(285 nm)/Si substrate. After that, a standard lithography process was exploited to define the channel areas, which were protected by photoresist during the removal of other WS_2 regions by oxygen plasma. Another lithography process was then used to define the source and drain areas, followed by the deposition of Bi/Au stacks (5 nm/80 nm) using thermal evaporation and the lift-off process. The performance of fabricated back-gated field-effect transistors (FETs) was evaluated in a vacuum probe station with a pressure smaller than 1×10^{-3} Pa. A semiconductor analyzer (B1500A, Keysight) was used to record the electrical data. The photodetection performance was assessed under ambient conditions. For the photodetection performance measurement, a 532 nm laser was employed, where its power was measured by an optical power meter (PM320E, Thorlabs) equipped with a Si diode photodetector (S130VC, Thorlabs).

3. Results and discussion

3.1. Morphology characterization

Here, (0001) oriented single side polished sapphire substrates were utilized for the CVD synthesis of WS_2. Due to the similar lattice symmetry between WS_2 and sapphire, it is feasible to realize epitaxial growth although they interact with each other by the weak van der Waals interaction. Under the optimal synthesis condition (*i.e.* with weight ratio of WO_3 and $Na_2WO_4 \bullet 2H_2O$ as 1:2, and reaction time of 40 min), large WS_2 triangular flakes with well-aligned orientations can be achieved as shown in **Fig. 1**a. Their size distribution is then extracted from Fig. 1a and depicted in Fig. 1b. Based on the normal distribution fitting, a mean value of 664 μm is obtained, suggesting the relatively large size of these triangular flakes. In fact, the largest WS_2 flakes can exceed 1 mm (Figure S2, Supporting Information). The well-aligned triangular flakes can be clearly seen from Fig. 1a. In order to illustrate the aligned orientation more accurately, the orientation distribution is extracted from Fig. 1a and presented in Fig. 1c. It is obvious that the flakes show four dominant orientations, indicating the epitaxial growth of WS_2 on sapphire substrate. Such large single crys-
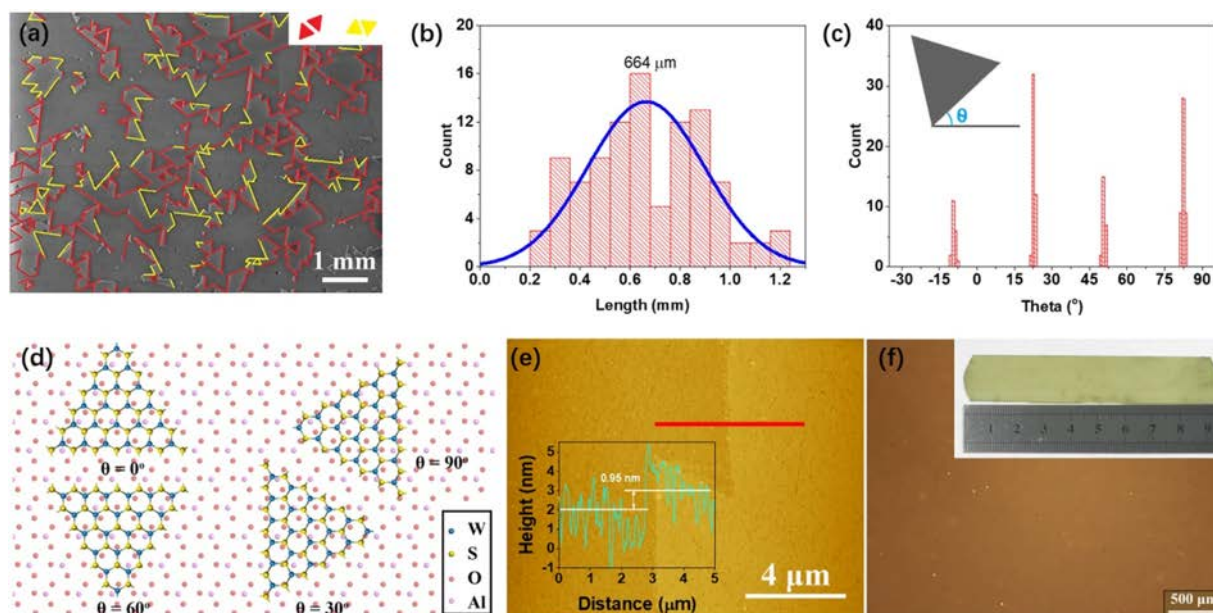
Fig. 1. Morphology, orientation and size distribution of the monolayer WS_2 flakes. (a) SEM image of the WS_2 flakes. The red lines and yellow lines indicate the WS_2 triangular grains with different orientations. Inset shows the schematic of the triangular grains with different orientations. (b) Size distribution of the triangular grains. (c) Orientation distribution of the WS_2 triangular grains. Inset illustrates the schematic of the determination of the theta value. (d) Schematic of the orientation relationship between WS_2 and sapphire substrate. (e) AFM image of a typical monolayer WS_2 flake. Inset presents the height profile along the edge indicated by the red line. (f) Optical microscope image of a continuous WS_2 film. Inset gives the digital photograph of a continuous WS_2 film.

tals with well-aligned orientations are reported for the first time to the best of our knowledge. The most probable relative orientation for the monolayer WS_2 grown on sapphire surface is schematically displayed in Fig. 1d. The 0° and 60° orientations correspond to the 3-on-2 superstructure of WS_2 and sapphire because the distance between adjacent S atoms of WS_2 is 3.18 Å and the distance between adjacent O atoms of Al_2O_3 is 4.81 Å. The similar phenomenon was also observed in the epitaxial growth of MoS_2 on sapphire [21,22]. On the other hand, there is not any strict lattice match for the other two orientations (*i.e.* 30° and 90°), which have similar atom alignments with the sapphire substrate. For determining the thickness of triangles flakes, AFM measurement was carried out. A typical AFM image of the WS_2 flake is shown in Fig. 1e. The WS_2 flake shows a thickness of 0.95 nm, corresponding to the monolayer of WS_2. For obtaining a continuous film, the longer growth time is implemented. In our experiments, a growth duration of 60 min is optimal for the growth of a continuous film (Fig. 1f). Remarkably, the centimeter scale continuous monolayer WS_2 film can be achieved, where the size of 1.7×9.5 cm^2 is displayed in the inset of Fig. 1f. It is anticipated that the wafer scale monolayer WS_2 film can be realized when a larger tube furnace is used.

3.2. Microstructure and crystallinity characterization

In order to evaluate the crystallinity of obtained WS_2 monolayer films, thorough TEM measurements were performed. A representative TEM image is shown in Fig. 2a. The observed cracks and triangular holes may be generated during the sample preparation. Notably, the uniform contrast of the film suggests the good uniformity of the grown film. High-resolution TEM images were also recorded to examine the crystal structure and crystallinity of the WS_2 film with the typical image given in Fig. 2b. It is evident that clear lattice fringes can be seen, designating the good crystallinity of the WS_2. Lattice spacings of 0.27 nm is observed (Fig. 2b), which corresponds to the spacing of the {100} planes of WS_2. It should also be noticed that during the HRTEM measurements, the WS_2 crystal

could be destroyed due to the strong electron-beam irradiation. In this way, the cracks shown in the image are most probably caused by the electron-beam damage. The high crystallinity of WS_2 can be confirmed by the selected area electron diffraction (SAED) measurements. As depicted in the typical SAED pattern in Fig. 2c, there is only one set of diffraction spots observed, indicating the single crystallinity of the detected area with the diffraction spots assigned to the {100} planes of WS_2. All these results can clearly reveal the excellent crystallinity of our WS_2 monolayer films.

3.3. Optical spectra characterization

After that, different optical spectra were collected to further characterize the as-synthesized WS_2 monolayer films. A typical Raman spectrum with characteristic peaks labelled corresponding to WS_2 is displayed in **Fig. 3**a. These sharp Raman peaks indicate the good crystallinity of the film, being consisting with the TEM results discussed above. Because of the close positions of the $2LA(M) - E^2_{2\,g}(\Gamma), E^1_{2\,g}(M), 2LA(M),$ and $E^1_{2\,g}(\Gamma)$ Raman modes, Lorentzian fitting is used to determine to exact peak positions as compiled and shown in Fig. 3a. In this way, the energy difference between $E^1_{2\,g}(\Gamma)$ and $A_{1g}(\Gamma)$ peaks is determined to be 59.3 cm^{-1}, signifying that the WS_2 film is indeed a monolayer film [23]. The strong $2LA(M)$ peak caused by the double resonance scattering is much stronger that of the $A_{1g}(\Gamma)$ peak in monolayer WS_2, further confirming the single layer of the WS_2 film [24]. Since monolayer WS_2 is a direct bandgap semiconductor, it should have strong photoluminescence (PL) peaks. Based on the collected PL signals as given in Fig. 3b, a strong PL peak is observed, again revealing that the obtained WS_2 is a single layer film. It is worth mentioning that the PL spectrum can be deconvoluted into four sub-peaks according to Lorentzian fitting, which are located at 1.884, 1.933, 1.977, and 2.006 eV, respectively. The peak located at 1.884 eV is attributed to the defects while the peak of 1.933 eV is ascribed to the biexciton/defect [25]. The peaks located at 1.977 and 2.006 eV are belonged to the signals of trion and exciton of monolayer WS_2, respectively [26,27]. After transferring the WS_2 film onto the SiO_2/Si
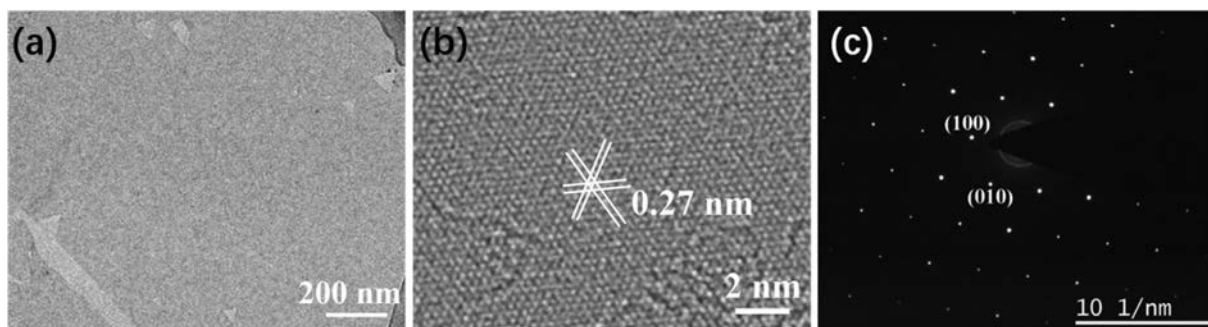
Fig. 2. TEM characterization of the obtained WS$_2$. (a) Low-magnified TEM image. (b) High-resolution TEM image. (c) SAED pattern.
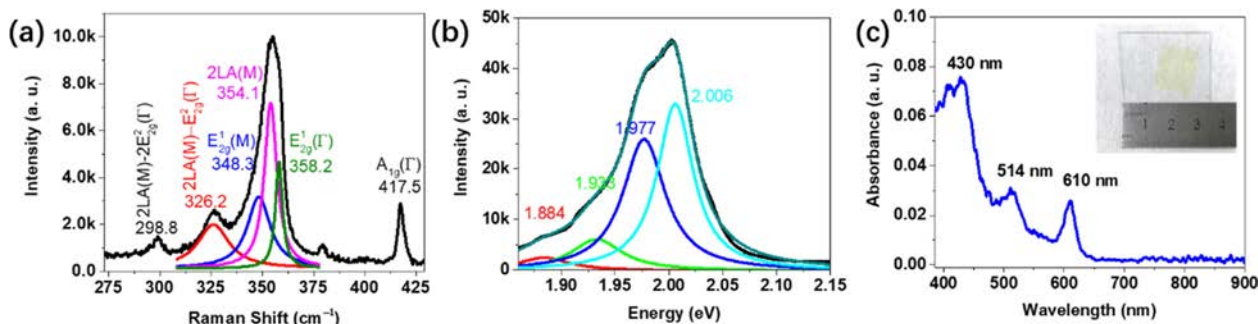
Fig. 3. Optical spectra of the monolayer WS$_2$. (a) Raman spectrum. The peaks are fitted by Lorentz function. (b) PL spectrum. The peaks are fitted by Lorentz function. (c) Absorbance spectrum. Inset shows the monolayer WS$_2$ film transferred onto a glass substrate. For Raman and PL measurements, a 532 nm laser was used as the excitation source.

substrate, the strain in WS$_2$ can be released, resulting in a blue shift of the PL peak (Figure S3, Supporting Information) [28]. As large-area WS$_2$ films were obtained here, it is convenient to measure the absorbance spectrum after the transfer of WS$_2$ onto the glass substrate as shown in the inset of Fig. 3c. The corresponding absorbance spectrum is presented in Fig. 3c. It is clear that there are three excitonic peaks observed that are positioned at 610, 514, and 430 nm. These absorption peaks are attributed to A, B, and C excitons in the monolayer WS$_2$, respectively [29]. Peak A is linked to the excitonic absorption in direct gap of WS$_2$ films, where it is located at the K valley of the Brillouin zone [30]. Therefore, the excitonic A peak should be correlated with the PL peak due to the same origin. The peak located at 610 nm is corresponded to the photon energy of 2.033 eV, which is perfectly consistent with the PL peak of monolayer WS$_2$ transferred onto the SiO$_2$/Si substrate, indicating the same origin of the peak. In addition, the energy difference between the excitonic peaks A and C is highly sensitive to the thickness of WS$_2$, in which it is usually used to determine the thickness of WS$_2$ films [29,30]. Based on the energy difference of 0.851 eV between these two excitonic peaks, it is again confirmed that the obtained WS$_2$ is a monolayer film [29].

3.4. Growth mechanism

To shed light on the growth mechanism of these large single crystal monolayer WS$_2$ epitaxial films, the growth behavior of WS$_2$ with varied growth parameters were carefully investigated. Because adding Na$_2$WO$_4$•2H$_2$O into the precursor is a key factor for the growth, the morphology evolution as a function of the weight ratio between WO$_3$ and Na$_2$WO$_4$•2H$_2$O was examined with the results compiled in **Fig. 4**. When a small amount of Na$_2$WO$_4$•2H$_2$O was mixed with WO$_3$, the growth became very slow with only a few dispersed small WS$_2$ flakes found on the substrate (Fig. 4a and 4b). In addition, the WS$_2$ flakes show the round-like shape when the weight ratio between WO$_3$ and Na$_2$WO$_4$ is 100:1, which

may be due to the ultra-slow growth rate. With the increasing amount of Na$_2$WO$_4$•2H$_2$O, the morphology of WS$_2$ changed into triangles as displayed in Fig. 4b. However, these triangular flakes have random orientations as confirmed by the corresponding orientation distribution (Figure S4a, Supporting Information). Once the amount of Na$_2$WO$_4$•2H$_2$O continued to increase, large triangular flakes with well-aligned orientations are witnessed (Fig. 4c-4g) with the respective orientation distributions compiled in Supporting Information Figure S3. These results designate that the addition of Na$_2$WO$_4$•2H$_2$O is beneficial for facilitating the epitaxial growth of WS$_2$ films. The average size of triangular flakes is found to gradually increase with the decreasing weight ratio between WO$_3$ and Na$_2$WO$_4$ (Fig. 4i-4l). However, the size of triangular flakes would start to decrease by further increasing the amount of Na$_2$WO$_4$ (Fig. 4h, 4k and 4l) even though the triangular flakes still exhibit well-defined orientations (see the statistical orientations shown in Figure S4, Supporting Information). Furthermore, there would not be any WS$_2$ flakes produced without the addition of WO$_3$. All these findings indicate that the amount of Na$_2$WO$_4$•2H$_2$O is important for controlling the morphology evolution of WS$_2$ monolayer films.

Simultaneously, the time evolution of the morphology of WS$_2$ films were also cautiously studied as illustrated in **Fig. 5**. In the early state of the growth, only small triangular WS$_2$ flakes are observed on the substrate (Fig. 5a). These small-size flakes show the epitaxial relation with the underlying substrate as witnessed from the orientation distribution of these triangular flakes (Fig. 5e). With the increasing growth time, these small triangular flakes gradually grow into the larger flakes (Fig. 5b and 5c, Figure S5a-S5c, Supporting Information) and finally merge into a continuous film (Fig. 5d). It is impressive that these triangular flakes maintain their epitaxial relationship with the substrate during the growth (Fig. 5e-5g). In fact, the nucleation density is found to decrease with the increasing growth time (Figure S5d, Supporting Information). The reduced density of nuclei and increased size of triangular flakes designate that the growth of the monolayer WS$_2$ trian-
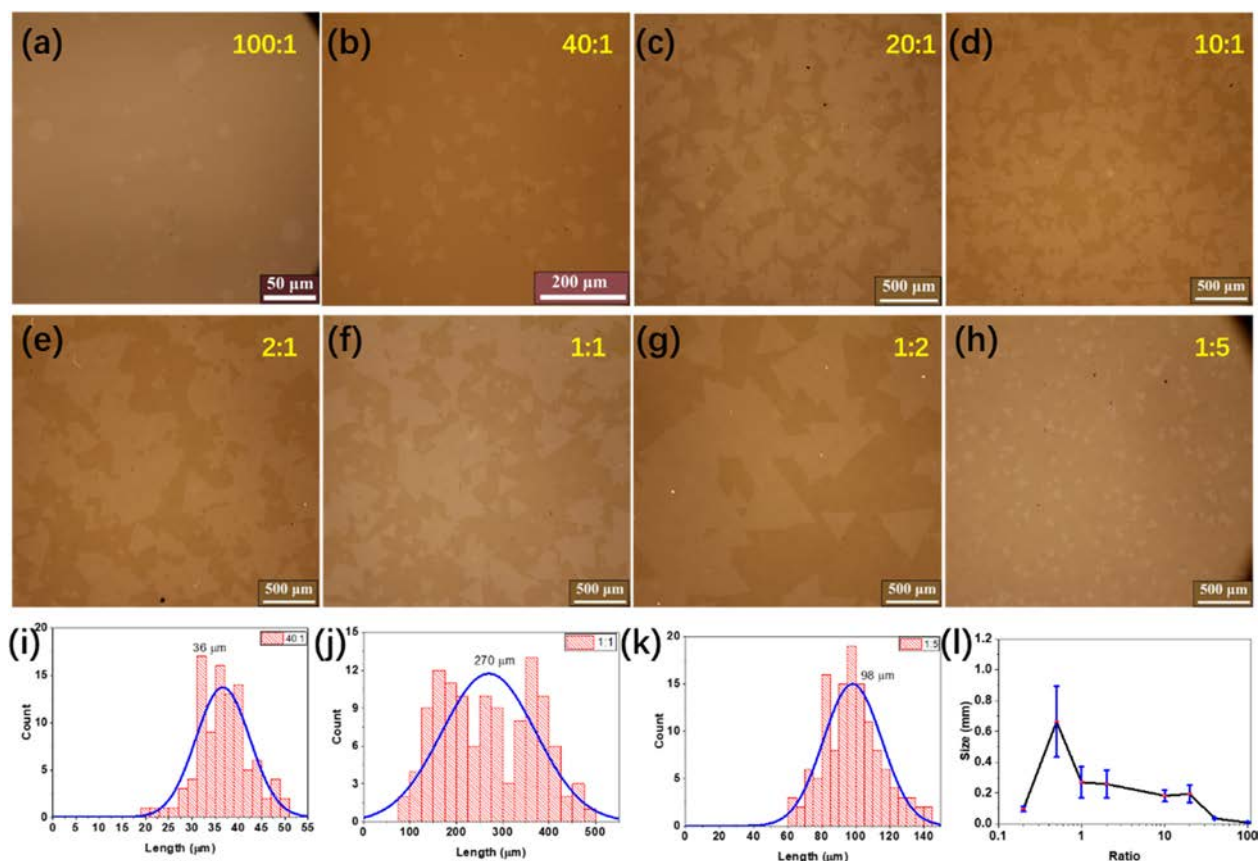
Fig. 4. Morphology and size evolution as a function of the weight ratio between WO_3 and Na_2WO_4. Optical microscope image of the samples. (a) 100:1, (b) 40:1, (c) 20:1, (d) 8:1, (e) 2:1, (f) 1:1, (g) 1:2, (h) 1:5. Size distribution of the WS_2 triangular flakes. (i) 40:1, (j) 1:1, (k) 1:5. (l) Size distribution of the flakes as a function of the weight ratio between WO_3 and $Na_2WO_4 \bullet 2H_2O$. The growth time is 40 min.
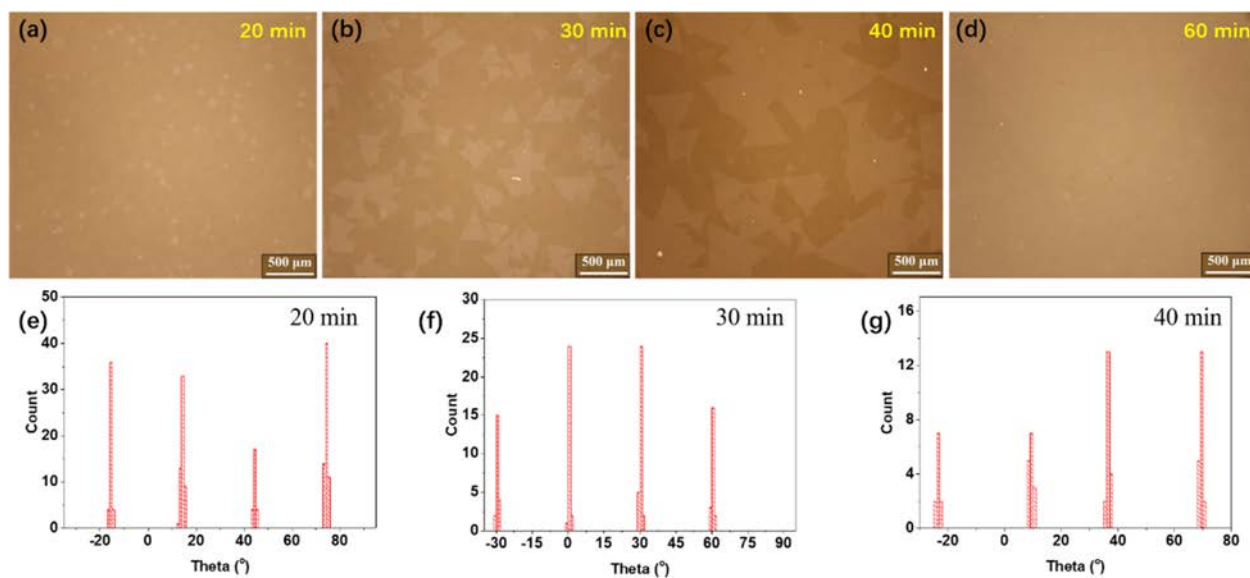
Fig. 5. Time evolution of the morphology of WS_2 monolayer films with the weight ratio of WO_3 and $Na_2WO_4 \bullet 2H_2O$ kept at 1:2. Optical microscope images of the samples. (a) 20 min, (b) 30 min, (c) 40 min, (d) 60 min. Orientation distributions of the samples. (e) 20 min, (f) 30 min, (g) 40 min.

gular flakes follows the mechanism of Ostwald ripening or Smolu-chowski ripening [31].

Based on the above discussion, a growth mechanism can be proposed for the Na_2WO_4-assisted growth of WS_2 monolayer films (Fig. 6). During the growth, it is anticipated that the mixture of WO_3 and $Na_2WO_4 \bullet 2H_2O$ would first change into liquid at high

temperatures since Na_2WO_4 has a relatively low melting point (698 °C). Then, there is a reaction occurred between Na_2WO_4 and WO_3, leading to the formation of liquid $Na_2W_xO_y$, where x and y indicate the atomic content relative to two Na atoms. This way, $Na_2W_xO_y$ would evaporate at high temperatures, delivering $Na_2W_xO_y$ vapor. As the $Na_2W_xO_y$ vapor is not stable, it will de-
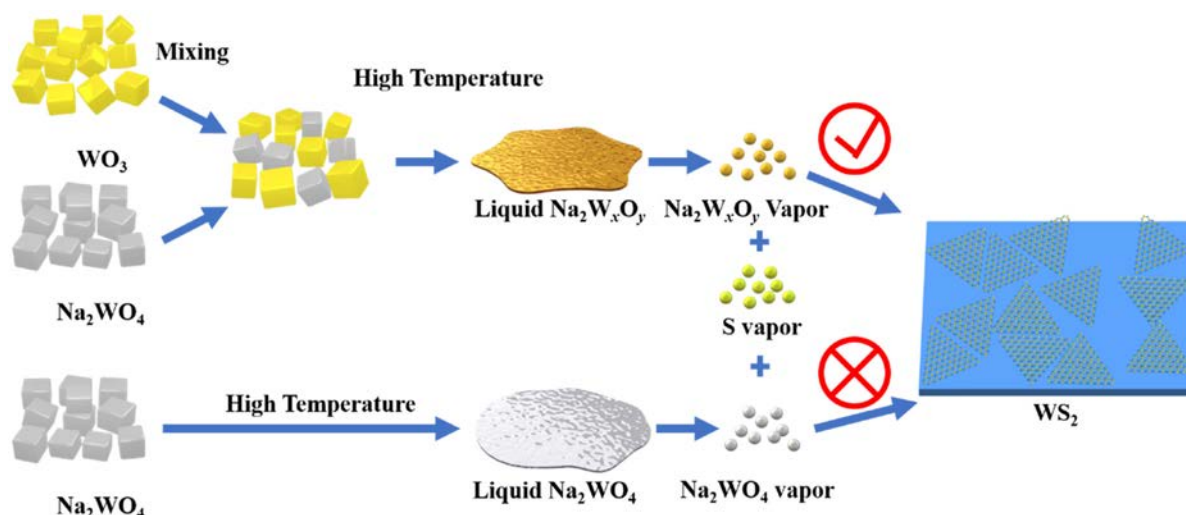
Fig. 6. Proposed growth mechanism of the monolayer WS_2 triangular flakes.

compose into Na_2WO_4 and WO_z. This hypothesis is supported by the thermogravimetry and differential scanning calorimetry analysis (Figure S6, Supporting Information). These newly formed WO_z species have the high chemical activity, which can react with S easily, forming WS_2 species and transporting to the substrate by the carrier gas. Once they hit the substrate, WS_2 seeds can be nucleated to form the triangular flakes. Due to the similar lattice symmetry between WS_2 and c-oriented sapphire, there is a possibility for the formation of van der Waals epitaxy, yielding well-aligned triangular WS_2 flakes on the substrate. As a result, the Na_2WO_4 species may have four functions here. Firstly, they can facilitate the continuous and stable feeding of WO_z species during the reaction. This is because the newly formed $Na_2W_xO_y$ liquid does not react with S directly. In fact, after the reaction, there is not any WS_2 but $Na_2W_xO_y$ observed in the precursor boat (Figure S7, Supporting Information). Furthermore, the $Na_2W_xO_y$ species can still be used for the synthesis of WS_2, which has been confirmed in our experiments, suggesting the validity of the hypothesis. Also, the $Na_2W_xO_y$ species cannot release WO_z because no WS_2 can be found on the substrate when using only Na_2WO_4 as the W source. The Na_2WO_4 precursor still remains as pure Na_2WO_4 after the reaction (Figure S8, Supporting Information). Secondly, the Na_2WO_4 species can provide homogeneous WO_z during the growth due to the reaction between Na_2WO_4 and WO_3. The evaporation of liquid $Na_2W_xO_y$ is a more stable process as compared to that of its solid powder. Thus, homogeneous $Na_2W_xO_y$ can be formed at high temperatures, which leads to the formation of homogeneous WO_z species. Thirdly, the existence of Na species may reduce the reaction barrier between WO_z and S, yielding the fast formation of WS_2 species, which has been reported for the growth of MoS_2 [32]. Fourthly, the $Na_2W_xO_y$ species may increase the interaction between WS_2 and sapphire, leading to the epitaxial growth of WS_2 on sapphire. Actually, the quasi-epitaxy between triangular WS_2 flakes and sapphire has been witnessed in our previous work using NaOH as a promoter [26], but the exact mechanism behind the phenomenon still needs further studies. In this case, the morphology evolution of WS_2 on the weight ratio between WO_3 and $Na_2WO_4 \cdot 2H_2O$ can be explained as the following. When the amount of Na_2WO_4 is low, the amount of WO_z species generated is low, inducing the slow growth speed and low growth yield of WS_2. In addition, the amount of Na species is relatively low in the region near the substrate, which is not sufficient for guiding the epitaxial growth of WS_2 on sapphire. As a result, randomly distributed triangular WS_2 flakes are formed. With the gradually increasing amount

of Na_2WO_4, the generated WO_z species would increase drastically, giving the dense nucleation and fast growth of the WS_2 flakes. Therefore, the dense triangular flakes with well-aligned orientations are obtained. The release of WO_z species should be similar for a wide range of weight ratio (*e.g.* 20 to 1) because the triangular flakes have the similar size as indicated in Fig. 4l. Further increasing the amount of Na_2WO_4 can reduce the amount of WO_z species as the index of y in $Na_2W_xO_y$ is close to 1. This way, once the nucleation density is reduced, the larger triangular WS_2 flakes are formed. When the amount of Na_2WO_4 increases too much, the release amount of WO_z species is drastically reduced. As a result, the growth rate of WS_2 is reduced with the formation of small WS_2 flakes. Recently, it was reported that graphene nanoribbons can be grown with two different edges by tuning the orientations of the nano-trenches on h-BN substrate [33]. However, due to the large lattice mismatch between WS_2 (3.18 Å) and h-BN (2.51 Å), it may be impossible to have a similar template growth behavior for WS_2. While due to the similar lattice symmetry, it is possible to realize van der Waal epitaxial growth of WS_2 monolayers on h-BN [34]. Further work is needed towards the growth of unidirectional large single domain WS_2 monolayers.

3.5. Electrical properties

Since WS_2 is considered as a potential candidate active material for next generation electronics, it is necessary to explore the electrical properties of as-synthesized WS_2 films. Here, global back-gated FETs are constructed using the monolayer WS_2 film as device channel as schematically presented in the inset of **Fig. 7**a. The SEM image of a representative FET is shown in Fig. 7a, which has a channel length (L) of 3.7 μm and width (W) of 79 μm. Because it has been reported that Bi contact is beneficial for the formation of ohmic contact between WS_2 and Bi [35], Bi contact is employed for our devices. The FET shows the typical n-type semiconducting properties as it can be seen from the transfer curves as shown in Fig. 7b and 7c, where the current increases with the increasing gate voltage. The on/off current ratio can then be determined from the logarithmic current plot (Fig. 7c), in which it is larger than 10^6, being comparable to the values reported in literatures (**Table 1**). The large hysteresis in the transfer curves may be caused by charge traps arising from various origins, such as the interface states existed between WS_2 channel and SiO_2 dielectric, defects in WS_2, and charge traps in the SiO_2 dielectric, *etc.* [36–39]. The corresponding output curves is given in Fig. 7d. The current in-
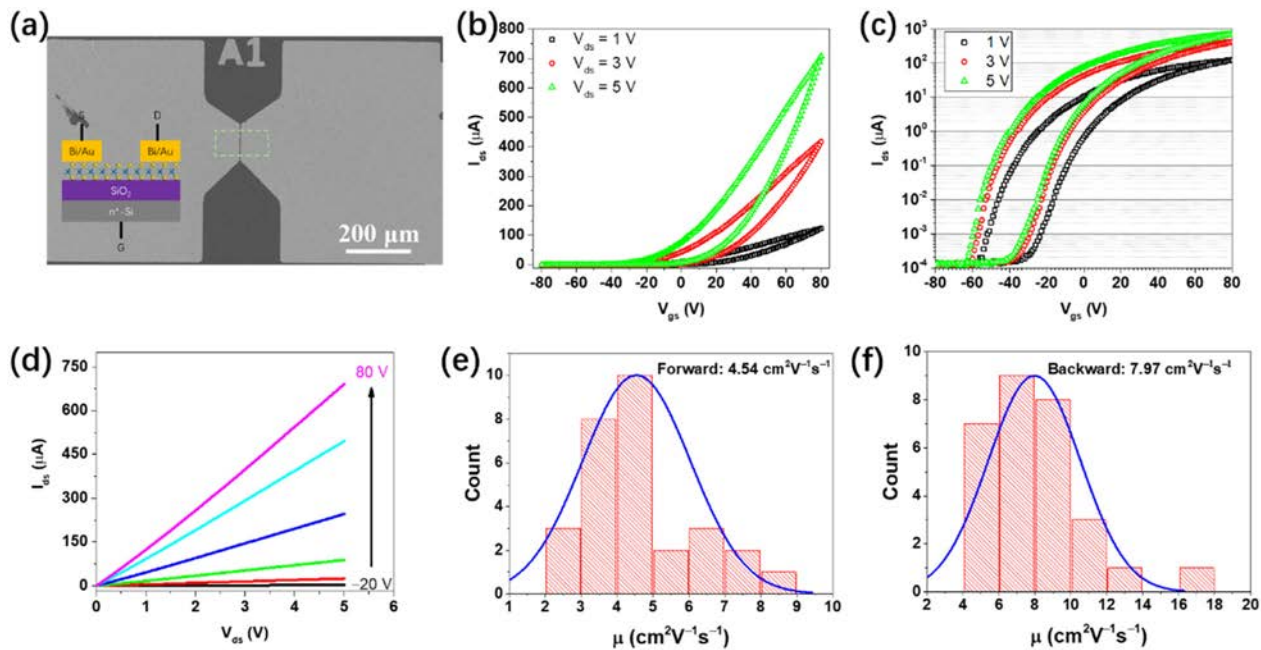
Fig. 7. Electrical properties of the obtained WS$_2$ films. (a) SEM image of a typical FET. The green dashed square indicates the WS$_2$ channel region. Inset shows the device schematic of the FET. (b) Transfer curves. (c) Transfer curves with the logarithmic current axis. (d) Output curves. (e) Statistical of mobility calculated from the transfer curve in the forward sweep. (f) Statistical of mobility calculated from the transfer curve in the backward sweep.

Table 1

Electrical properties of monolayer WS$_2$ films synthesized by different CVD methods.

Single domain size(μm)	Mobility(cm$^2 \bullet V^{-1} \bullet s^{-1}$)		On/off current ratio	Maximum current density(μA/μm)	Ref.
~40	6		10^6	35	[40]
~500	4 – 14		$10^7 – 10^8$	~0.15	[14]
~233	32.3		10^6	7.3	[41]
Mean: 576 Maximum: ~1000	1–2		~10^7	~2	[15]
~420	20		~10^8	~1	[42]
300 – 400	~6		~10^5	~0.24	[43]
Maximum:	Forward maximum	8.2	>10^6	8.7	Our
1200	Forward mean	4.54			work
Mean:	Backward maximum	16.7			
664	Backward mean	7.97			

creases with the increasing gate voltage, being consisting with the transfer curves. The linear output curves (I_{ds}–V_{ds} curves) suggest the ohmic-like electrical contact formed between metals electrode and device channels for the efficient carrier transport and extraction. Thus, an on current density of 8.7 μA/μm is obtained, which is considered to be relatively high among different state-of-the-art WS$_2$ devices (Table 1). Based on the output curves, it can be inferred that the device operates in the linear regime. In this regard, the mobility of the FETs can be estimated using the following analytical equation:

$$\mu = \frac{\partial I_{ds}}{\partial V_{gs}} \cdot \frac{L}{W} \cdot \frac{1}{C_{ox} V_{ds}} \tag{1}$$

where C_{ox} is the gate capacitance per unit area (*i.e.* 1.21 $\times$ 10^{-4} F m^{-2} for 285 nm thick SiO$_2$). In this way, the mobility of the device demonstrated in Fig. 7b is calculated to be 7.0 and 12.4 cm^{2}V^{-1}s^{-1} for the forward and backward sweepings, respectively. To assess the uniformity of the electrical performance of the WS$_2$ film, tens of FETs were configured and the statistics of the extracted mobility of these FETs are compiled in Fig. 7e and 7f. The mean mobility is 4.54 cm^{2}V^{-1}s^{-1} for the forward sweeping, while it increases to 7.97 cm^{2}V^{-1}s^{-1} for the backward sweeping. These values are already comparable with the ones of CVD-synthesized monolayer WS$_2$ films reported in other recent works (Table 1), suggesting the good crystal quality of our WS$_2$ films.

3.6. Optoelectronic properties

Apart from FETs, WS$_2$ is also a good optoelectronic material with promising applications for optoelectronic devices. In this work, the photodetection performance of the obtained WS$_2$ films is explored. The I_{ds}–V_{ds} curves with and without light irradiation of the device is shown in **Fig. 8**a. It is obvious that the device current increases with the increasing light intensity, indicating the good photosensitivity of WS$_2$. In order to have a deeper understanding of the device characteristics, photocurrent (I_p) *vs.* light intensity (Φ) was measured and is depicted in Fig. 8b. It is seen that the photocurrent increases with the increasing light intensity, which is perfectly consistent with the I_{ds}–V_{ds} curves as shown in Fig. 8a. The relationship between photocurrent and light intensity can be well fitted by a sublinear equation of

$$I_p = A\Phi^\alpha \tag{2}$$

where A and α are the fitting parameters. Based on the fitting from the measured data, α is found to be 0.77. This sublinear relationship of the photocurrent with respect to light intensity is caused by the complex generation, trapping, and recombination processes of the photogenerated carriers, which are always observed in semiconductors based photoconductive detectors [44–46]. Moreover, responsivity is an important figure of merit for evaluating the perfor-
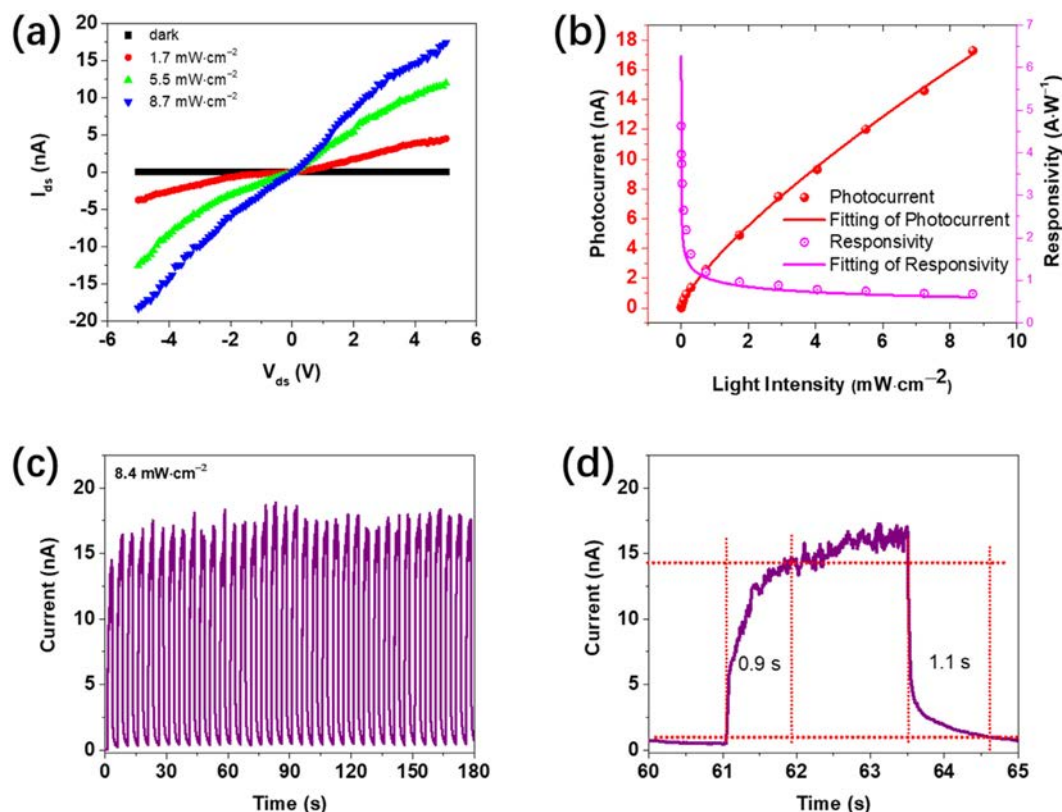
Fig. 8. Optoelectronic properties of the obtained WS$_2$ films. (a) Current-voltage curves without and with the light illumination. (b) Photocurrent and responsivity as a function of light intensity. (c) Time-dependent current under the chopped light illumination. (d) Time-dependent current showing the determination of rise and decay time constants. The wavelength of the light illumination is 532 nm.

mance of a photodetector, which is defined as

$$R = \frac{I_p}{\Phi S} \qquad (3)$$

where S is the sensitive area of the photodetector (*i.e.* 292.3 μm^2 for the studied device as shown in Fig. 8). The calculated R as a function of light intensity is displayed in Fig. 8b. According to Eq. (2) and (3), the responsivity R should be proportional to $\Phi^{\alpha-1}$ that is proportional to $\Phi^{-0.23}$. Thus, the responsivity decreases with the increasing light intensity. A maximum responsivity of 4.6 A W^{-1} is obtained when the light intensity is 3.3×10^{-4} mW cm^{-2}. With the increasing light intensity, the responsivity would reach a saturation value of 0.68 A W^{-1}. This high responsivity at the low light intensity is caused by charge traps, which are frequently observed in low-dimensional materials based photoconductive detectors [47–49]. At this low light intensity, photogenerated holes are trapped by defects, the recombination rate of photogenerated electrons is reduced, leading to the increase of photogenerated electron lifetime (τ). Also, the gain (G) of a photoconductive detector is known as $G = \tau/t_{tr}$, where t_{tr} is the transit time of electrons between electrodes. Therefore, the gain would increase at the low light intensity, leading to the increase of responsivity. At the high light intensity, most of the traps are filled by photogenerated holes, resulting in the increased recombination rate of photogenerated electrons. In this way, the responsivity reduces accordingly. Another important parameter is specific detectivity (D^*), which can be written as $D^* = R\cdot(S/2qI_{dark})$ if we consider the main noise is from shot noise here. q is the charge of an electron while I_{dark} is the dark current of the photodetector. According to the formula, D^* is proportional to R, where the highest D^* is determined to be 2.2×10^{12} Jones. The D^* will reach a saturation value of 3.3×10^{12} Jones under the high light intensity (Fig-

ure S9, Supporting Information). More importantly, the operation stability of a photodetector under modulated light irradiation is essential for practical applications. As shown in Fig. 8c, the stable on- and off-state current under modulated light illumination are witnessed, confirming the excellent stability of the device. The high-resolution current-time curve is as well shown in Fig. 8d, which is used to determine the response speed of the photodetector. The rise and decay time constants are defined as the time interval for photocurrent varied from 10 to 90% and vise visa, respectively. Accordingly, the rise and decay time constants are found to be 0.9 ad 1.1 s, respectively. These photodetection parameters are already comparable or even better than the values reported in literatures (Table 2). This respectable photodetection performance clearly suggests the potential of our monolayer WS$_2$ films for next-generation optoelectronics.

4. Conclusion

In summary, epitaxial monolayer WS$_2$ films with ultra-large single crystal domains are successfully synthesized by the modified CVD method. These high quality WS$_2$ monolayer films are characterized by optical microscopy, SEM, TEM, and optical spectroscopies in details. It is found that the introduction of Na$_2$WO$_4$ in the precursor is extremely important to achieve large single domains of WS$_2$ with well-aligned epitaxial relationship with underlying sapphire substrates. Importantly, when configured into back-gated FETs, they demonstrate large electron mobilities with a mean mobility of 4.54 cm^{2}V^{-1}s^{-1} for the forward sweeping and a mean mobility of 7.97 cm^{2}V^{-1}s^{-1} for the backward sweeping, being comparable to other state-of-the-art CVD grown WS$_2$ devices. These devices also exhibit respectable photodetection performance with a maximum photoresponsivity of 4.7 A W^{-1}. All these results sug-

Table 2

Performance Parameters of photodetectors based on monolayer WS_2.

Electrode	V_{ds} (V)	V_{gs} (V)	Channel length (μm)	Environment	Wavelength (nm)	R (A W^{-1})	D* (Jones)	Speed (s)	Ref.
Graphene	5	0	0.2	Ambient	532	2.5	9.9×10^{10}	–	[50]
Au	4	0	0.2	Ambient	532	20	–	–	[51]
Graphene	5	30	1	Ambient	532	121	–	–	[52]
Ti/Au	2	0	2	Vacuum	532	3.2×10^{-3}	–	0.17	[26]
Bi/Au	5	0	3.7	Ambient	532	4.6	2.2×10^{12}	1.1	This work

gest that the modified CVD method here does not only provide a facile platform for the synthesis of high quality, large single crystal, epitaxial monolayer WS2 films, but also facilitates their excellent intrinsic materials properties for next-generation electronics and optoelectronics.

Appendix. Supplementary data

Supplementary data associated with this article can be found, in the online version, at

Declaration of Competing Interest

The authors declare that they have no known competing financial interests or personal relationships that could have appeared to influence the work reported in this paper.

CRediT authorship contribution statement

Changyong Lan: Conceptualization, Methodology, Investigation, Validation, Writing – original draft, Writing – review & editing, Supervision, Funding acquisition. **Rui Zhang:** Investigation, Visualization. **Haolun Wu:** Investigation, Visualization. **Shaofeng Wen:** Investigation, Visualization. **Ruisen Zou:** Investigation. **Xiaolin Kang:** Investigation. **Chun Li:** Conceptualization, Supervision, Writing – review & editing, Funding acquisition. **Johnny C. Ho:** Conceptualization, Supervision, Writing – review & editing, Funding acquisition. **Yi Yin:** Writing – review & editing. **Yong Liu:** Writing – review & editing.

Acknowledgements

Supplementary materials

Supplementary material associated with this article can be found, in the online version, at doi:10.1016/j.apmt.2021.101232.

References

[1] C.N. Lau, F. Xia, L. Cao, Emergent quantum materials, MRS Bull. 45 (2020) 340–347, doi:10.1557/mrs.2020.125.

[2] Y. Liu, X. Duan, H.-J. Shin, S. Park, Y. Huang, X. Duan, Promises and prospects of two-dimensional transistors, Nature 591 (2021) 43–53, doi:10.1038/s41586-021-03339-z.

[3] S.-.K. Su, C.-.P. Chuu, M.-.Y. Li, C.-.C. Cheng, H.-S.P. Wong, L.-J. Li, Layered semiconducting 2D materials for future transistor applications, Small Struct 2 (2021) 2000103, doi:10.1002/sstr.202000103.

[4] M. Long, P. Wang, H. Fang, W. Hu, Progress, challenges, and opportunities for 2D material based photodetectors, Adv. Funct. Mater. 29 (2019) 1803807, doi:10.1002/adfm.201803807.

[5] M. Xu, T. Liang, M. Shi, H. Chen, Graphene-like two-dimensional materials, Chem. Rev. 113 (2013) 3766–3798, doi:10.1021/cr300263a.

[6] S.J. Kim, K. Choi, B. Lee, Y. Kim, B.H. Hong, Materials for flexible, stretchable electronics: graphene and 2D materials, Annu. Rev. Mater. Res. 45 (2015) 63–84, doi:10.1146/annurev-matsci-070214-020901.

[7] J. Jiang, N. Li, J. Zou, X. Zhou, G. Eda, Q. Zhang, H. Zhang, L.-J. Li, T. Zhai, A.T. Wee, Synergistic additive-mediated CVD growth and chemical modification of 2D materials, Chem. Soc. Rev. 48 (2019) 4639–4654, doi:10.1039/C9CS00348G.

[8] L. Tang, J. Tan, H. Nong, B. Liu, H.-.M. Cheng, Chemical Vapor Deposition Growth of Two-Dimensional Compound Materials: controllability, Material Quality, and Growth Mechanism, Acc. Mater. Res. 2 (2020) 36–47, doi:10.1021/accountsmr.0c00063.

[9] L. Zhang, J. Dong, F. Ding, Strategies, Status, and Challenges in Wafer Scale Single Crystalline Two-Dimensional Materials Synthesis, Chem. Rev. 121 (2021) 6321–6372, doi:10.1021/acs.chemrev.0c01191.

[10] X. Xu, Z. Zhang, J. Dong, D. Yi, J. Niu, M. Wu, L. Lin, R. Yin, M. Li, J. Zhou, S. Wang, J. Sun, X. Duan, P. Gao, Y. Jiang, X. Wu, H. Peng, R.S. Ruoff, Z. Liu, D. Yu, E. Wang, F. Ding, K. Liu, Ultrafast epitaxial growth of metre-sized single-crystal graphene on industrial Cu foil, Sci. Bull. 62 (2017) 1074–1080, doi:10.1016/j.scib.2017.07.005.

[11] H. Yu, M. Liao, W. Zhao, G. Liu, X. Zhou, Z. Wei, X. Xu, K. Liu, Z. Hu, K. Deng, S. Zhou, J.-.A. Shi, L. Gu, C. Shen, T. Zhang, L. Du, X. Xie, J. Zhu, W. Chen, R. Yang, D. Shi, G. Zhang, Wafer-scale growth and transfer of highly-oriented monolayer MoS$_2$ continuous films, ACS Nano 11 (2017) 12001–12007, doi:10.1021/acsnano.7b03819.

[12] Q. Wang, N. Li, J. Tang, J. Zhu, Q. Zhang, Q. Jia, Y. Lu, Z. Wei, H. Yu, Y. Zhao, Y. Guo, L. Gu, G. Sun, W. Yang, R. Yang, D. Shi, G. Zhang, Wafer-scale highly oriented monolayer MoS$_2$ with large domain sizes, Nano Lett. 20 (2020) 7193–7199, doi:10.1021/acs.nanolett.0c02531.

[13] C. Lan, C. Li, J.C. Ho, Y. Liu, 2D WS2: from vapor phase synthesis to device applications, Adv. Electron. Mater. 7 (2020) 2000688, doi:10.1002/aelm.202000688.

[14] S. Zhou, S. Liu, S. Cui, X. Ping, D. Hu, L. Jiao, Fast growth of large single-crystalline WS$_2$ monolayers via chemical vapor deposition, Nano Res. 14 (2021) 1659–1662, doi:10.1007/s12274-020-2859-9.

[15] Y. Gao, Z. Liu, D.-.M. Sun, L. Huang, L.-.P. Ma, L.-.C. Yin, T. Ma, Z. Zhang, X.-.L. Ma, L.-.M. Peng, H.-.M. Cheng, W. Ren, Large-area synthesis of high-quality and uniform monolayer WS$_2$ on reusable Au foils, Nat. Commun. 6 (2015) 8569, doi:10.1038/ncomms9569.

[16] H.G. Ji, Y.-.C. Lin, K. Nagashio, M. Maruyama, P. Solís-Fernández, A. Sukma Aji, V. Panchal, S. Okada, K. Suenaga, H. Ago, Hydrogen-assisted epitaxial growth of monolayer tungsten disulfide and seamless grain stitching, Chem. Mater. 30 (2018) 403–411, doi:10.1021/acs.chemmater.7b04149.

[17] M. Chubarov, T.H. Choudhury, D.R. Hickey, S. Bachu, T. Zhang, A. Sebastian, A. Bansal, H. Zhu, N. Trainor, S. Das, M. Terrones, N. Alem, J.M. Redwing, Wafer-Scale Epitaxial Growth of Unidirectional WS$_2$ Monolayers on Sapphire, ACS Nano 15 (2021) 2532–2541, doi:10.1021/acsnano.0c06750.

[18] J. Zhou, J. Lin, X. Huang, Y. Zhou, Y. Chen, J. Xia, H. Wang, Y. Xie, H. Yu, J. Lei, D. Wu, F. Liu, Q. Fu, Q. Zeng, C.-.H. Hsu, C. Yang, L. Lu, T. Yu, Z. Shen, H. Lin, B.I. Yakobson, Q. Liu, K. Suenaga, G. Liu, Z. Liu, A library of atomically thin metal chalcogenides, Nature 556 (2018) 355–359, doi:10.1038/s41586-018-0008-3.

[19] C. Lan, C. Li, Y. Yin, Y. Liu, Large-area synthesis of monolayer WS$_2$ and its ambient-sensitive photo-detecting performance, Nanoscale 7 (2015) 5974–5980, doi:10.1039/C5NR01205H.

[20] G.F. Schneider, V.E. Calado, H. Zandbergen, L.M. Vandersypen, C. Dekker, Wedging transfer of nanostructures, Nano Lett. 10 (2010) 1912–1916, doi:10.1021/nl1008037.

[21] D. Dumcenco, D. Ovchinnikov, K. Marinov, P. Lazic, M. Gibertini, N. Marzari, O.L. Sanchez, Y.-.C. Kung, D. Krasnozhon, M.-.W. Chen, S. Bertolazzi, P. Gillet, A.F. i. Morral, A. Radenovic, A. Kis, Large-area epitaxial monolayer MoS$_2$, ACS Nano 9 (2015) 4611–4620, doi:10.1021/acsnano.5b01281.

[22] K. Suenaga, H.G. Ji, Y.-.C. Lin, T. Vincent, M. Maruyama, A.S. Aji, Y. Shiratsuchi, D. Ding, K. Kawahara, S. Okada, V. Panchal, O. Kazakova, H. Hibino, K. Suenaga, H. Ago, Surface-mediated aligned growth of monolayer MoS$_2$ and in-plane heterostructures with graphene on sapphire, ACS Nano 12 (2018) 10032–10044, doi:10.1021/acsnano.8b04612.

[23] C. Cong, J. Shang, X. Wu, B. Cao, N. Peimyoo, C. Qiu, L. Sun, T. Yu, Synthesis and optical properties of large-area single-crystalline 2D semiconductor WS$_2$ monolayer from chemical vapor deposition, Adv. Opt. Mater. 2 (2014) 131–136, doi:10.1002/adom.201300428.

[24] A. Berkdemir, H.R. Gutiérrez, A.R. Botello-Méndez, N. Perea-López, A.L. Elías, C.-.I. Chia, B. Wang, V.H. Crespi, F. López-Urías, J.-.C. Charlier, H. Terrones, M. Terrones, Identification of individual and few layers of WS$_2$ using Raman spectroscopy, Sci. Rep. 3 (2013) 1755, doi:10.1038/srep01755.

[25] Y. Zhu, H. Yi, Q. Hao, J. Liu, Y. Ke, Z. Wang, D. Fan, W. jing Zhang, Scalable synthesis and defect modulation of large monolayer WS$_2$ via annealing in H$_2$S atmosphere/thiol treatment to enhance photoluminescence, Appl. Surf. Sci. 485 (2019) 101–107, doi:10.1016/j.apsusc.2019.04.168.

[26] C. Lan, X. Kang, R. Wei, Y. Meng, S. Yip, H. Zhang, J.C. Ho, Utilizing a NaOH promoter to achieve large single-domain monolayer WS$_2$ films via modified chemical vapor deposition, ACS Appl. Mater. Interfaces 11 (2019) 35238–35246, doi:10.1021/acsami.9b12516.

[27] C. Lan, D. Li, Z. Zhou, S. Yip, H. Zhang, L. Shu, R. Wei, R. Dong, J.C. Ho, Direct visualization of grain boundaries in 2D monolayer WS$_2$ via induced growth of CdS nanoparticle chains, Small Methods 3 (2019) 1800245, doi:10.1002/smtd.201800245.

[28] Y. Wang, C. Cong, W. Yang, J. Shang, N. Peimyoo, Y. Chen, J. Kang, J. Wang, W. Huang, T. Yu, Strain-induced direct–indirect bandgap transition and phonon modulation in monolayer WS$_2$, Nano Res. 8 (2015) 2562–2572, doi:10.1007/s12274-015-0762-6.

[29] B. Zhu, X. Chen, X. Cui, Exciton binding energy of monolayer WS$_2$, Sci. Rep. 5 (2015) 9218, doi:10.1038/srep09218.

[30] W. Zhao, Z. Ghorannevis, L. Chu, M. Toh, C. Kloc, P.-.H. Tan, G. Eda, Evolution of electronic structure in atomically thin sheets of WS$_2$ and WSe$_2$, ACS Nano 7 (2013) 791–797, doi:10.1021/nn305275h.

[31] X. Zhang, T.H. Choudhury, M. Chubarov, Y. Xiang, B. Jariwala, F. Zhang, N. Alem, G.-.C. Wang, J.A. Robinson, J.M. Redwing, Diffusion-controlled epitaxy of large area coalesced WSe$_2$ monolayers on sapphire, Nano Lett. 18 (2018) 1049–1056, doi:10.1021/acs.nanolett.7b04521.

[32] P. Yang, X. Zou, Z. Zhang, M. Hong, J. Shi, S. Chen, J. Shu, L. Zhao, S. Jiang, X. Zhou, Y. Huan, C. Xie, P. Gao, Q. Chen, Q. Zhang, Z. Liu, Y. Zhang, Batch production of 6-inch uniform monolayer molybdenum disulfide catalyzed by sodium in glass, Nat. Commun. 9 (2018) 979, doi:10.1038/s41467-018-03388-5.

[33] H.S. Wang, L. Chen, K. Elibol, L. He, H. Wang, C. Chen, C. Jiang, C. Li, T. Wu, C.X. Cong, T.J. Pennycook, G. Argentero, D. Zhang, K. Watanabe, T. Taniguchi, W. Wei, Q. Yuan, J.C. Meyer, X. Xie, Towards chirality control of graphene nanoribbons embedded in hexagonal boron nitride, Nat. Mater. 20 (2021) 202–207, doi:10.1038/s41563-020-00806-2.

[34] J.S. Lee, S.H. Choi, S.J. Yun, Y.I. Kim, S. Boandoh, J.-.H. Park, B.G. Shin, H. Ko, S.H. Lee, Y.-.M. Kim, Y.H. Lee, K.K. Kim, S.M. Kim, Wafer-scale single-crystal hexagonal boron nitride film via self-collimated grain formation, Science 362 (2018) 817–821, doi:10.1126/science.aau2132.

[35] P.-.C. Shen, C. Su, Y. Lin, A.-.S. Chou, C.-.C. Cheng, J.-.H. Park, M.-.H. Chiu, A.-.Y. Lu, H.-.L. Tang, M.M. Tavakoli, G. Pitner, X. Ji, Z. Cai, N. Mao, J. Wang, V. Tung, J. Li, J. Bokor, A. Zettl, C.-.I. Wu, T. Palacios, L.-.J. Li, J. Kong, Ultralow contact resistance between semimetal and monolayer semiconductors, Nature 593 (2021) 211–217, doi:10.1038/s41586-021-03472-9.

[36] C. Lan, X. Kang, Y. Meng, R. Wei, X. Bu, S. Yip, J.C. Ho, The origin of gate bias stress instability and hysteresis in monolayer WS$_2$ transistors, Nano Res. 13 (2020) 3278–3285, doi:10.1007/s12274-020-3003-6.

[37] C. Lan, S. Yip, X. Kang, Y. Meng, X. Bu, J.C. Ho, Gate Bias Stress Instability and Hysteresis Characteristics of InAs Nanowire Field-Effect Transistors, ACS Appl. Mater. Interfaces 12 (2020) 56330–56337, doi:10.1021/acsami.0c17317.

[38] A. Di Bartolomeo, L. Genovese, F. Giubileo, L. Iemmo, G. Luongo, T. Foller, M. Schleberger, Hysteresis in the transfer characteristics of MoS$_2$ transistors, 2D Mater. 5 (2017) 015014, doi:10.1088/2053-1583/aa91a7.

[39] C. Lee, S. Rathi, M.A. Khan, D. Lim, Y. Kim, S.J. Yun, D.-.H. Youn, K. Watanabe, T. Taniguchi, G.-.H. Kim, Comparison of trapped charges and hysteresis behavior in hBN encapsulated single MoS$_2$ flake based field effect transistors on SiO$_2$ and hBN substrates, Nanotechnology 29 (2018) 335202, doi:10.1088/1361-6528/aac6b0.

[40] V.K. Singh, R. Pendurthi, J.R. Nasr, H. Mamgain, R.S. Tiwari, S. Das, A. Srivastava, Study on the Growth Parameters and the Electrical and Optical Behaviors of 2D Tungsten Disulfide, ACS Appl. Mater. Interfaces 12 (2020) 16576–16583, doi:10.1021/acsami.9b19820.

[41] Y. Yue, J. Chen, Y. Zhang, S. Ding, F. Zhao, Y. Wang, D. Zhang, R. Li, H. Dong, W. Hu, Y. Feng, W. Feng, Two-dimensional high-quality monolayered triangular WS$_2$ flakes for field-effect transistors, ACS Appl. Mater. Interfaces 10 (2018) 22435–22444, doi:10.1021/acsami.8b05885.

[42] S.J. Yun, S.H. Chae, H. Kim, J.C. Park, J.-.H. Park, G.H. Han, J.S. Lee, S.M. Kim, H.M. Oh, J. Seok, M.S. Jeong, K.K. Kim, Y.H. Lee, Synthesis of centimeter-scale monolayer tungsten disulfide film on gold foils, ACS Nano 9 (2015) 5510–5519, doi:10.1021/acsnano.5b01529.

[43] A. Zafar, Z. Zafar, W. Zhao, J. Jiang, Y. Zhang, Y. Chen, J. Lu, Z. Ni, Sulfur-mastery: precise synthesis of 2D transition metal Dichalcogenides, Adv. Funct. Mater. 29 (2019) 1809261, doi:10.1002/adfm.201809261.

[44] C. Lan, R. Dong, Z. Zhou, L. Shu, D. Li, S. Yip, J.C. Ho, Large-scale synthesis of freestanding layer-structured PbI$_2$ and MAPbI$_3$ nanosheets for high-performance photodetection, Adv. Mater. 29 (2017) 1702759, doi:10.1002/adma.201702759.

[45] D. Li, C. Lan, A. Manikandan, S. Yip, Z. Zhou, X. Liang, L. Shu, Y.-.L. Chueh, N. Han, J.C. Ho, Ultra-fast photodetectors based on high-mobility indium gallium antimonide nanowires, Nat. Commun. 10 (2019) 1664, doi:10.1038/s41467-019-09606-y.

[46] H. Zhang, W. Wang, S. Yip, D. Li, F. Li, C. Lan, F. Wang, C. Liu, J.C. Ho, Enhanced performance of near-infrared photodetectors based on InGaAs nanowires enabled by a two-step growth method, J. Mater. Chem. C 8 (2020) 17025–17033, doi:10.1039/D0TC04330C.

[47] C. Lan, F. Li, S. Yip, R. Wei, X. Kang, X. Bu, R. Dong, H. Zhang, J.C. Ho, Direct vapor–liquid–solid synthesis of all-inorganic perovskite nanowires for high-performance electronics and optoelectronics, ACS Nano 13 (2019) 6060–6070, doi:10.1021/acsnano.9b02379.

[48] D. Li, S. Yip, F. Li, S. Yip, R. Wei, X. Bu, X. Kang, C. Lan, C. Liu, J.C. Ho, Flexible Near-Infrared InGaSb Nanowire Array Detectors with Ultrafast Photoconductive Response Below 20 μs, Adv. Opt. Mater. 8 (2020) 2001201, doi:10.1002/adom.202001201.

[49] F. Li, Y. Meng, R. Dong, S. Yip, C. Lan, X. Kang, F. Wang, K.S. Chan, J.C. Ho, High-performance transparent ultraviolet photodetectors based on InGaZnO superlattice nanowire arrays, ACS Nano 13 (2019) 12042–12051, doi:10.1021/acsnano.9b06311.

[50] H. Tan, Y. Fan, Y. Zhou, Q. Chen, W. Xu, J.H. Warner, Ultrathin 2D photodetectors utilizing chemical vapor deposition grown WS$_2$ with graphene electrodes, ACS Nano 10 (2016) 7866–7873, doi:10.1021/acsnano.6b03722.

[51] Y. Fan, Y. Zhou, X. Wang, H. Tan, Y. Rong, J.H. Warner, Photoinduced Schottky barrier lowering in 2D monolayer WS$_2$ photodetectors, Adv. Opt. Mater. 4 (2016) 1573–1581, doi:10.1002/adom.201600221.

[52] T. Chen, Y. Sheng, Y. Zhou, R.-j. Chang, X. Wang, H. Huang, Q. Zhang, L. Hou, J.H. Warner, High photoresponsivity in ultrathin 2D lateral graphene: WS$_2$: graphene photodetectors using direct CVD growth, ACS Appl. Mater. Interfaces 11 (2019) 6421–6430, doi:10.1021/acsami.8b20321.